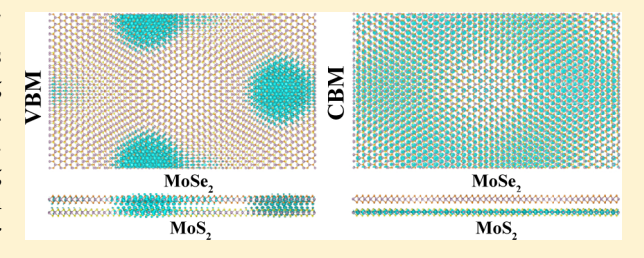


# Electronic Structural Moiré Pattern Effects on MoS<sub>2</sub>/MoSe<sub>2</sub> 2D Heterostructures

Jun Kang, †,‡ Jingbo Li,† Shu-Shen Li,† Jian-Bai Xia,† and Lin-Wang Wang\*,‡

Supporting Information

**ABSTRACT:** The structural and electronic properties of  $MoS_2/MoSe_2$  bilayers are calculated using first-principles methods. It is found that the interlayer van der Waals interaction is not strong enough to form a lattice-matched coherent heterostructure. Instead, a nanometer-scale Moiré pattern structure will be formed. By analyzing the electronic structures of different stacking configurations, we predict that the valence-band maximum (VBM) state will come from the  $\Gamma$  point due to interlayer electronic coupling. This is confirmed by a direct calculation of a



Moiré pattern supercell containing 6630 atoms using the linear scaling three-dimensional fragment method. The VBM state is found to be strongly localized, while the conduction band minimum (CBM) state is only weakly localized, and it comes from the  $MoS_2$  layer at the K point. We predict such wave function localization can be a general feature for many two-dimensional (2D) van der Waals heterostructures and can have major impacts on the carrier mobility and other electronic and optical properties.

KEYWORDS: 2D heterostructure, lattice incommensurateness, Moiré pattern, wave function localization

wo-dimensional (2D) semiconducting transition-metal dichalcogenides (sTMDs), such as MoS<sub>2</sub> and MoSe<sub>2</sub>, have received considerable attention owing to their extraordinary fundamental physical properties and application potentials in electronic devices. <sup>1-6</sup> In conventional semiconductors, it is well-established that heterostructures can be used to engineer their electronic properties. The successful isolation of various 2D materials in recent years<sup>7,8</sup> has raised the possibility of designing van der Waals 2D heterostructures with enormous variability in terms of material choice and layer thickness. For example, graphene/BN heterostructures are already experimentally achievable via either transfer processes<sup>9,10</sup> or epitaxial growth.<sup>11</sup> WSe<sub>2</sub> layers have also been grown sandwiching rocksalt structure PbSe layers, forming different types of multiple-layer 2D heterostructures. 12 In a recent review by Geim and Grigorieva, 13 such van der Waals 2D heterostructures are predicted to be the next wave of research beyond the current single graphene sheet. Meanwhile, interesting physics has been theoretically predicted in many 2D heterostructures, such as localization of Dirac electrons in rotated graphene bilayers, <sup>14</sup> metallic electronic properties in graphene/MoS<sub>2</sub> superlattices, <sup>15</sup> and electron—hole pair separation 16 and high photovoltaic performance 17 in MoS<sub>2</sub>/WS<sub>2</sub> heterojunctions. Compared to conventional semiconductor heterostructures, van der Waals 2D heterostructures are relatively easy to make (e.g., using Scotch tape technology<sup>18</sup>) and have atomically sharp interfaces. One reason for this fact is the lack of requirement for lattice matching between different 2D layers due to the weak van der Waals interaction and the

lack of coherent covalent bonds between the 2D layers. This, however, also raises an issue: how such lattice incommensurateness between different 2D layers will affect their electronic structures and optical properties. As a matter of fact, the 2D layers can also be rotated by almost any arbitrary angle with respect to each other. This increases the variability of such 2D heterostructure design but also creates intriguing questions for their electronic and transport properties: in terms of wave function localization, carrier mobility, electron—phonon coupling, and so forth. In general, lattice mismatched or rotated 2D heterostructures will show a Moiré pattern viewing from the top. It is thus the purpose of the current work to show the effects of such Moiré pattern on the electronic structures of a 2D heterostructure by using the MoS<sub>2</sub>/MoSe<sub>2</sub> double-layer as an example.

Recently, several theoretical studies on the electronic structure of  $MoS_2/MoSe_2$  heterostructures have been reported. In these works the lattice mismatch between  $MoS_2$  and  $MoSe_2$  was ignored, and the monolayers were artificially compressed or stretched to form a common lateral lattice. However, as we will show later in this paper, the van der Waals binding energy between the  $MoS_2$  and  $MoSe_2$  layers is not strong enough to force a coherence lattice between these two layers, and hence a nanometer-scale Moiré pattern will form. In a Moiré pattern, the stacking configurations in

Received: August 15, 2013 Revised: September 26, 2013

<sup>&</sup>lt;sup>†</sup>State Key Laboratory of Superlattices and Microstructures, Institute of Semiconductors, Chinese Academy of Sciences, P.O. Box 912, Beijing 100083, China

<sup>\*</sup>Materials Sciences Division, Lawrence Berkeley National Laboratory, Berkeley, California 94720, United States

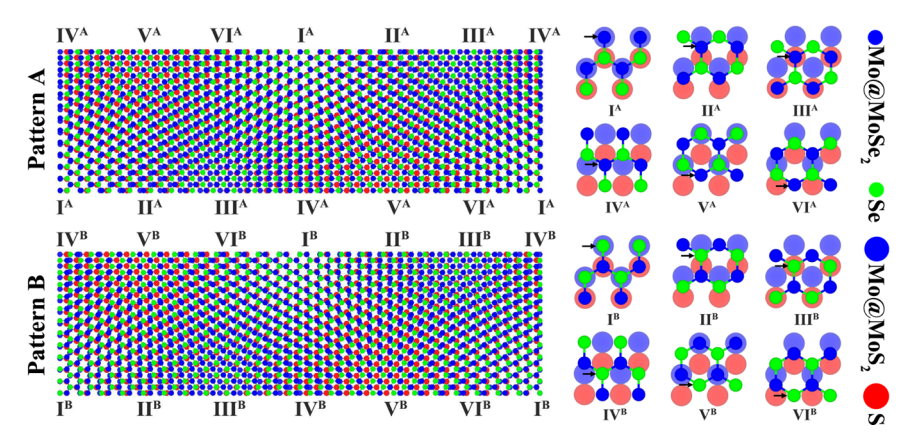


Figure 1. (Left) Moiré patterns A and B with 4.4% lattice mismatch corresponding to  $24 \times 24 \text{ MoS}_2$  and  $23 \times 23 \text{ MoSe}_2$  supercells along the primary cell lattice vectors. We have taken a rectangular supercell (which contains two  $24 \times 24/23 \times 23$  supercells) for linear scaling DFT calculation. Only half (in (n,0) direction) of the rectangular periodic supercell is shown above to denote different stacking regions. (Right) The 12 different stacking configurations considered (with MoSe<sub>2</sub> on top of MoS<sub>2</sub>). Between consecutive configurations within  $I^A$ – $VI^A$  or  $I^B$ – $VI^B$ , the MoSe<sub>2</sub> layer is translated along the (n,n) direction in steps of  $3(a/6)^{1/2}$ , where a is the lattice constant, which is fixed at the average of the values for the MoSe<sub>2</sub> and MoSe<sub>2</sub> monolayers. The arrows indicate the same atom in the MoSe<sub>2</sub> layer in  $I^A$ – $VI^A$  or  $I^B$ – $VI^B$ . Configurations  $I^A$ – $VI^A$  cover the A pattern, and configurations  $I^B$ – $VI^B$  cover the B pattern.

Table 1. Layer Distance d and Adsorption Energy E<sub>ad</sub> per Formula Unit (Each MoSe<sub>2</sub>/MoS<sub>2</sub>) for Different Configurations

	$I^A$	$II^A$	$III^A$	$IV^A$	$V^{A}$	$VI^A$	$I^B$	$II^B$	$III^{B}$	$IV^B$	$V^{B}$	$VI^B$
d (Å)	3.72	3.48	3.08	3.22	3.12	3.45	3.12	3.43	3.77	3.48	3.16	3.25
$E_{\rm ad}~({ m meV})$	118	141	195	174	191	141	194	143	120	140	177	170

different regions are different, which results in spatially varying interlayer coupling strength and electrostatic potential. One intrinsic question that will be addressed in the current study is whether or not such spatial variation can cause wave function localization. If so, what is the cause of such localization: is it due to coupling variation or electrostatic potential variation? We will use first-principles calculations to study these problems. In particular, we will first analyze the effects of stacking differences by calculating different stacking patterns, then calculate a whole 6630 atom Moiré pattern system with a linear scaling density functional theory (DFT) method. We find that the Moiré pattern effect is strong enough to localize the hole wave function due to wave function coupling variation, while the electron wave function is weakly localized due to electrostatic potential variation. The band structure also changes from a direct band gap system in monolayer MoS<sub>2</sub> or MoSe<sub>2</sub>, to an indirect band gap system much like in a multiple MoS2 or a multiple MoSe<sub>2</sub> layer system. The effects of Moiré patterns suggest potential new ways to engineer the electronic structures of such systems for possible future applications.

In the current study, we will mainly focus on systems without arbitrary in-plane angular rotations. As a result, there are only two possible Moiré patterns A and B, as shown in Figure 1, with their in-plane hexagonal edges aligned in the same orientation and with a 4.4% lattice mismatch. As a matter of fact, one pattern can also be considered as a result of the other by a rotation of 60° of the top MoSe<sub>2</sub> layer. In each Moiré pattern, the local stacking geometry can be classified into six different types as I<sup>A</sup> to VI<sup>A</sup> or I<sup>B</sup> to VI<sup>B</sup> respectively, as shown in Figure 1. To study the effect of each stacking pattern, we have constructed small periodic systems using the average lattice constant 3.25 Å of MoS<sub>2</sub> and MoSe<sub>2</sub> to make them lattice matched. The calculations for these small systems (right panel of Figure 1) are performed using the Vienna ab initio simulation package (VASP). <sup>21,22</sup> The generalized gradient

approximation of Perdew–Burke–Ernzerhof (GGA-PBE)<sup>23</sup> is adopted for the exchange-correlation functional. The energy cutoff for plane-wave expansion is set to 400 eV. Brillouin zone sampling is performed with 12  $\times$  12  $\times$  1 Monkhorst–Pack (MP) special k-point meshes<sup>24</sup> including the  $\Gamma$ -point. A vacuum layer larger than 10 Å is added to avoid interaction between adjacent images. All atoms are allowed to be relaxed in the perpendicular z-direction until the atomic Hellmann–Feynman forces are smaller than 0.01 eV/Å. Spin–orbital coupling (SOC) is taken into account, and the effect of van der Waals interaction is included by using the empirical correction scheme of Grimme. According to a recent study, the interlayer structural and energetic properties of transition metal dichalcogenides such as  $\mathrm{MoS}_2$  can be represented accurately by the Grimme method.

In the I<sup>A</sup> configuration, the Mo and Se atoms in the MoSe<sub>2</sub> layer are on top of the Mo and S atoms in the MoS2 layer, respectively, while in the I<sup>B</sup> configuration, the Mo and Se atoms in the MoSe<sub>2</sub> layer are on top of the S and Mo atoms in the  $MoS_2$  layer, respectively. Starting from the  $I^A$  ( $I^B$ ) configuration, the other configurations (before relaxation)  $II^A - VI^A$  ( $II^B - VI^B$ ) can be obtained by translating the top MoSe<sub>2</sub> layer along the (n,n) (hexagonal primary cell direction index) direction (downward direction in Figure 1) in a step of  $3(a/6)^{1/2}$  for each translation (where a is the lateral lattice constant). The adsorption energies per formula unit (each MoSe<sub>2</sub>/MoS<sub>2</sub>) and interlayer Se and S atom vertical height differences (after atomic relaxation) for different stacking configurations are listed in Table 1. The most stable configuration is III<sup>A</sup>, with an adsorption energy of 195 meV, followed by IB (194 meV) and V<sup>A</sup> (191 meV). In these configurations, the Se atoms are on top of the hollow sites of the MoS2 layer. Configurations with Se atoms on top of the S atoms, namely, IA and IIIB, have the lowest adsorption energies. The Se and S atom interlayer vertical height difference in different configurations varies from

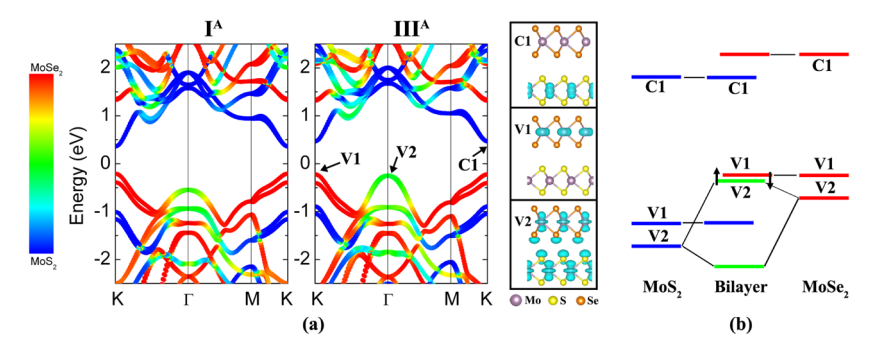


Figure 2. (a) Band structures of the  $I^A$  and  $III^A$  bilayers. Blue and red denote the contributions from  $MoS_2$  and  $MoSe_2$  layers, respectively. The partial charge densities of C1, V1, and V2 states of  $III^A$  are also shown. (b) Schematic of the band alignment between  $MoS_2$  and  $MoSe_2$  and the coupling effect for the V2 state in  $III^A$ . The arrows denote the eigenenergy shift of V1 and V2 states when  $MoS_2$  and  $MoSe_2$  layers relax to their natural lattice constants from the average lattice constant.

3.08 to 3.77 Å and has a reverse linear relationship with respect to the adsorption energy.

Although in many cases Moiré patterns can be formed based on synthesis kinetics (e.g., the mechanical exfoliation method), it might still be interesting to discuss its formation based on total energy consideration, as done in ref 27, especially for synthesis methods based more on thermodynamics. 11,12 In the MoS<sub>2</sub>/MoSe<sub>2</sub> bilayer, if a lattice-matched structure is formed, the system can have the maximum adsorption energy using stacking pattern IIIA; on the other hand, it will cost elastic energy due to lattice deformation. For a Moiré pattern heterostructure, the adsorption energy will be the average of the different stacking patterns (from I<sup>A</sup> to VI<sup>A</sup> or from I<sup>B</sup> to VI<sup>B</sup>), which turns out to be 160 meV per formula unit for Moiré pattern A and 157 meV for Moiré pattern B. These are 35 and 37 meV less than the adsorption energy of configuration III<sup>A</sup> and I<sup>B</sup> respectively. On the other hand, the strain energy to stretch MoS<sub>2</sub> to the average lattice constant (from 3.18 to 3.25 Å) is 37 meV per formula unit according to DFT calculations, and to compress MoSe<sub>2</sub> (from 3.32 to 3.25 Å) is 42 meV per formula unit. Hence, the total strain energy (79 meV per formula unit) is much larger than the gain in the adsorption energy. As a result, a lattice-mismatched Moiré-pattern structure will be formed.

The formation of Moiré patterns can lead to interesting electronic structures in MoS<sub>2</sub>/MoSe<sub>2</sub> bilayer. To gain a better understanding, we first look at the electronic structures of the different stacking patterns listed in Figure 1. In the following, we will focus on Moiré pattern A, expecting similar qualitative results for Moiré pattern B. The overall band structures of all the stacking configurations are similar, and those of IA and IIIA are illustrated in Figure 2. Due to the absence of inversion symmetry, the band structure shows significant spin-orbit splitting that does not appear in pure  $MoS_2$  or  $MoSe_2$  bilayers. The current results have a direct band gap at the K point, much like in the single-layer structure. To show the interlayer electron coupling, the projected weights of the MoS<sub>2</sub> and MoSe<sub>2</sub> layers to the electron wave function at a given kpoint and band state are denoted by colors in Figure 2a. It can be seen that the interlayer coupling is negligible to the band edge states around the K point. This happens because, in monolayer MoS<sub>2</sub> and MoSe<sub>2</sub>, the band edge states at the K points are mainly localized at the central Mo layer. The highest valence band state at the K point (V1) is contributed only by the MoSe<sub>2</sub> layer, while the lowest conduction band state (C1) is contributed only by the MoS<sub>2</sub> layer. This observation is

consistent with a type II band alignment between MoS2 and MoSe<sub>2</sub> as shown schematically in Figure 2b, obtained by aligning the band energies of the single layer MoS<sub>2</sub> and MoSe<sub>2</sub> with respect to the vacuum level.<sup>29</sup> The charge density plot of the V1 and C1 states are shown in Figure 2a. It is also notable that the highest valence band at the  $\Gamma$  point (V2) has significant contributions from both the MoS<sub>2</sub> and MoSe<sub>2</sub> layers (green color), which is consistent with its charge density plot in Figure 2a. This indicates that there is a strong interlayer electroncoupling effect for the V2 state. As we can see from Figure 2a, at different stacking (e.g., IA and IIIA), such a coupling effect can be rather different, and the coupling strength is largest when the interlayer Se and S vertical height distance is the smallest (stacking III<sup>A</sup>). The coupling tends to push the V2 energy up as schematically shown in Figure 2b. For example, in a single-layer MoSe<sub>2</sub> at the average lattice constant (3.25 Å) the energy difference between V1 and V2 is 0.58 eV, while in the heterostructure in III<sup>A</sup> the energy difference is only 0.03 eV. One must be cautious because the V1 and V2 levels in III<sup>A</sup> are very close, and thus their order could potentially be changed by higher-level computational methods (e.g., GW). Nevertheless, it was found under DFT calculation<sup>4</sup> that, if in the bilayers consisted with the same materials (e.g., two MoS<sub>2</sub> layers, or two MoSe<sub>2</sub> layers), then V2 is above V1 in agreement with experiments, which provides a test for the reliability of the theoretical calculation. In our case, one can further estimate the effect when the MoSe<sub>2</sub> and MoS<sub>2</sub> layers relax to their natural lattice constants in a Moiré pattern. This can be done by calculating the absolute lateral lattice deformation potentials  $E^{\rm DP}={
m d} \bar{E(\varepsilon)}/{
m d} \varepsilon$ , where  $\varepsilon=(a-a_0)/a_0$  ( $a_0$  is the equilibrium lattice constant) and  $E(\varepsilon)$  is the energy of the band edge state relative to the vacuum level at a certain  $\varepsilon$ . According to our calculation, the  $E^{DP}$  of V1 and V2 states in MoSe<sub>2</sub> are -5.0 and 3.3 eV, respectively. Therefore, when relaxed from the average lattice constant in stacking IIIA, the V1 state energy will shift downward by 0.11 eV, while the V2 will shift upward by 0.07 eV or slightly smaller value due to its MoS<sub>2</sub> component. Thus, according to this analysis, the V2 state in the III<sup>A</sup> region will become the top of valence band of the whole system.

To verify the above prediction from the analysis of the stacking patterns, we have calculated a whole Moiré pattern system using the linear scaling three-dimensional fragment (LS3DF) method.<sup>30</sup> The LS3DF method divides the system into fragments and then calculates each fragment and patches them into the original system with novel boundary cancellation techniques. The Coulomb potential, based on the global charge

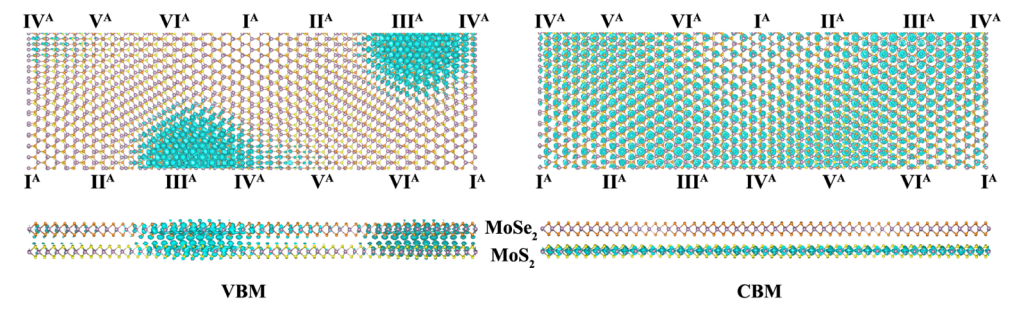
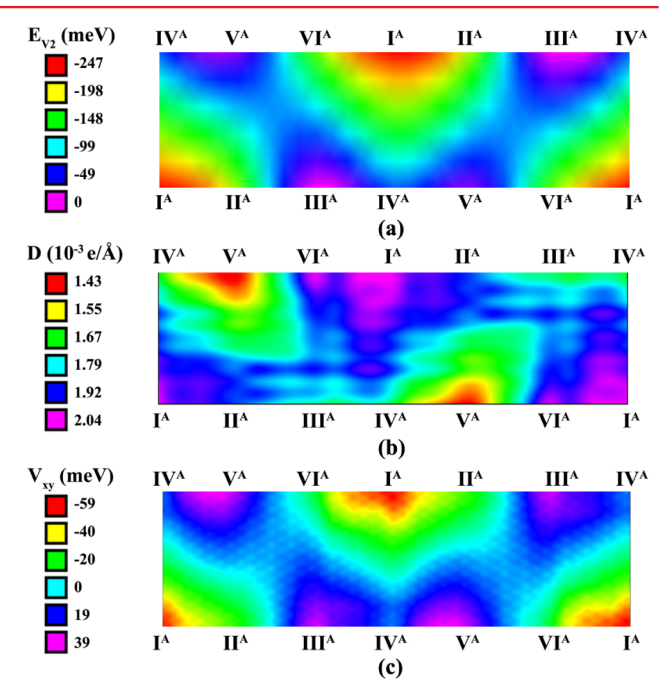


Figure 3. Top view and side view of the spatial distribution of the VBM, VBM-1 (left), and CBM (right) states for the Moiré structure A shown in Figure 1.

density, is solved on the whole system, and it thus includes all the self-consistent effects. It yields almost the same results as do direct DFT calculations. The comparison of the band structures of small systems in Figure 1, calculated by VASP and the PEtot package<sup>31</sup> upon which the LS3DF method is based, is included in the Supporting Information, from which we can see that VASP and PEtot (hence LS3DF) give almost the same band structures for the small systems. We have taken a rectangular supercell of Moiré pattern A (which contains two 24 × 24  $MoS_2$  and 23 × 23  $MoSe_2$  supercells with 6630 atoms in total) for LS3DF calculations. The interlayer distances in different regions of the structure are determined by an interpolation scheme from the values of the IA-VIA stacking patterns calculated above. A test shows that the eigenenergy error due to the interpolation scheme for the atomic displacement is less than 15 meV (see the Supporting Information). The LS3DF method yields the total charge density and total potential. The folded spectrum method (FSM)<sup>32</sup> is used to calculate the VBM and CBM states of the whole system based on LS3DF-obtained total potential (hence the single particle Hamiltonian). Normconserving pseudopotentials and plane wave basis sets are used in both the LS3DF and FSM calculations with a 60 Ryd plane wave energy cutoff, and spin-orbit coupling is included in the FSM calculation. The calculated VBM and VBM-1 (degenerated) states are shown in Figure 3. It can be seen that the VBM is indeed strongly localized in the III<sup>A</sup> region as predicted from the stacking pattern analysis. In addition, the VBM states distribute in both MoS<sub>2</sub> and MoSe<sub>2</sub> layers, much like the V2 state shown in Figure 2. This confirms that the VBM state of the whole system is V2 from the III<sup>A</sup> region, as predicted above. To further illustrate this point, we plot the distribution of the energy of the V2 state in Figure 4a, based on the calculations of I<sup>A</sup>-VI<sup>A</sup>. We align the energies of the V2 states (Figure 2a) in I<sup>A</sup>–VI<sup>A</sup> of Figure 1b by taking the average of the vacuum levels at the two sides of the bilayer and using that as a common energy reference. Then we do an interpolation to obtain the landscape of the energy of the V2 state in the Moiré pattern, as shown in Figure 4a. Indeed, the energy of V2 is highest in III<sup>A</sup>, where the VBM of the whole system localizes. It is also interesting to note that localization of Dirac electrons is observed in rotated bilayer graphene with small twist angles (~3°). 14,33,34 Rotation in bilayer graphene also forms Moiré patterns, and small twist angles can lead to large pattern domains, much like the Moiré pattern caused by small lattice mismatches. But the origin of the wave function localization for graphene bilayer and the MoS<sub>2</sub>/MoSe<sub>2</sub> bilayer here differs. In graphene, the localization is related to the overlap of the displaced Dirac cones which results in van Hove singularities.<sup>3</sup> In contrast, the localization in the MoS<sub>2</sub>/MoSe<sub>2</sub> bilayer is



**Figure 4.** Distribution of the energy of the V2 state based on the calculations of  $I^A$ – $VI^A$  (a), the planar-averaged dipole moment D (b), and z-integrated local potential  $V_{xy}$  (c) in Moiré pattern A.

caused by different coupling strengths at different regions of the pattern, and there is no Dirac cone in the electronic structure.

The situation of the CBM state is quite different, and its charge density is shown in Figure 3. It is distributed in the MoS<sub>2</sub> layer only, and it agrees with the C1 state at the K point as shown in Figure 2. The CBM wave function is only weakly localized. As there is no interlayer coupling (the wave function is localized within one layer), the weak localization must be caused by electrostatic potential variations. Plotting the electrostatic potentials separately for the two layers would be a direct way to understand the results. However, due to the vertical atomic displacement at difference places (warping), the finite real space numerical grid used, and the extremely large atomic potentials (which overwhelm the small electrostatic variation), it turns out to be numerically difficult to do a proper averaging and to plot the potentials in the two layers separately. Therefore we have adopted an alternative approach to analyze the potential. We first calculate the charge difference  $\Delta \rho(x, y, y)$ z) between the Moiré structure and isolated MoS<sub>2</sub> and MoSe<sub>2</sub> layers, with their atomic positions taken from the bilayer positions. Then the x-y planar-averaged electron charge difference  $\Delta \rho_{\text{ave}}(z)$  within each unit cell of the MoS<sub>2</sub> layer is

calculated. The vertical-direction dipole moment due to the charge transfer is then calculated as  $D = -\int \Delta \rho_{ave}(z)z \,dz$ , with the zero of z defined at the center of the bilayer. This stackingdependent dipole moment is shown in Figure 4b. A positive dipole moment will mean an electron charge flow from the MoSe<sub>2</sub> layer to the MoS<sub>2</sub> layer, hence a higher MoS<sub>2</sub> CBM position. As a result, the CBM will be localized at the smallest D regions in the Moiré pattern, which agrees with the CBM localization shown in Figure 3. Another possible charge transfer is in the lateral direction. However, due to the highly atomic oscillation behavior, the possible lateral charge transfer in  $\Delta \rho(x)$ (y, z) is hard to identify. Instead, we have calculated the lateral potential averaged in the z direction:  $V_{xy} = \int [V(x, y, z)/L_z] dz$ , with V being the local potential of the system, and  $L_z$  the length of the periodic box in the z direction. This  $V_{xy}$  potential is then smoothed by a Gaussian convolution in the x,y directions to remove the atomic oscillations. The resulting potential is shown in Figure 4c. Note that any z-direction dipole moment effect will be canceled out during the z-direction average. Thus,  $V_{xy}$ should be caused by the lateral charge transfer. According to this, the CBM should be localized in the negative  $V_{xy}$  region, that is, at I<sup>A</sup>. This is just the opposite of the z direction dipole moment effect. Judging from Figure 3b, at the end, it is the z direction dipole moment which determines the CBM localization.

Moreover, due to a type-II band alignment as shown in Figure 2b, the overall band gap of the bilayer system has been reduced from the monolayer band gap. In the Moiré pattern system, the first few VB state eigen energies are: 2.765, 2.765, 2.748, 2.747, and 2.712 eV, and the first few CB state eigen energies are: 3.960, 3.960, 3.976, 3.978, and 3.980 eV. Thus the overall band gap is 1.20 eV. In comparison, using the same parameters as in the LS3DF calculation, the PEtot-calculated single layer  $MoS_2$  band gap is 1.65 eV, and single-layer  $MoS_2$  band gap is 1.36 eV.

Finally, we would like to discuss the cases where the angle  $\theta$ between the crystallographic axes of the two atomic layers is not 0° or 60°. As we mentioned before, using mechanical exfoliation, systems with an arbitrary  $\theta$  can be constructed. In the Supporting Information we show Moiré patterns with different  $\theta$ . For small  $\theta$ , a similar Moiré pattern exists, while the size of the pattern decreases with increasing  $\theta$  value. We also show that similar VBM localization exists for other small  $\theta$ Moiré patterns. We note that a more complicated incoherent pattern might be formed if the 2D crystal structures of the two constituent layers are different. For example, in ref 12, hexagonal WSe2 layers can be grown on top of thin cubic PbSe layers. The patterning of such structures can be dense, in a way more like the large- $\theta$ -angle pattern shown in the Supporting Information. It will be interesting to study the electronic-structure consequences of such complex patterning in the future.

In summary, we have studied the adhesion and electronic properties of the  $MoS_2/MoSe_2$  bilayer. The adsorption energies for different stacking configurations were calculated, and it was demonstrated that the van der Waals interaction between these two layers was not strong enough to make a lattice-coherent heterostructure; instead a Moiré pattern would be formed. By analyzing the electronic structures of different stacking configurations within the Moiré pattern, we predict that the VBM state of the whole Moiré pattern system will come from the  $\Gamma$  point V2 state in region III^A due to interlayer coupling. This is later confirmed by direct LS3DF calculation of the

Moiré structure. The direct LS3DF calculation also shows that the CBM state is weakly localized. Through the electrostatic potential analysis, we found that the CBM localization was caused by a competition between the vertical charge-transfercaused dipole moment and a lateral charge-transfer-caused zaveraged potential difference at different regions. In the end, it is the vertical charge-transfer dipole moment which causes the weak CBM localization. Although it is not possible to define an exact k-point due to the loss of periodicity in the length scale of one unit cell, one can still use the k-points of the original unit cell (Figure 2) to characterize the wave function phase information over several unit cells (e.g., within the localization size region). In that sense, the VBM is in the  $\Gamma$  point, and CBM is in the K point. Thus, the MoS<sub>2</sub>/MoSe<sub>2</sub> bilayer will have an indirect band gap. This is similar to the MoS<sub>2</sub> or MoSe<sub>2</sub> doublelayer cases. Finally, we believe Moiré pattern-induced wave function localization will be a general feature for many future van der Waals 2D heterostructures. Since the energy separation of the VBM and CBM to the next VB and CB states are in the same order as the room temperature  $k_BT$ , we expect the localization effect will have significant impact on the system's carrier mobility and other electronic properties even at room temperature (especially when the carrier concentration is small). On the other hand, such patterned electron wave function localization also provides opportunities for the designs of future novel applications. Such features and the large number of possible Moiré patterns can only exist in 2D systems and thus provide opportunities for future research. At this point, it is extremely interesting to confirm the existence of the localized state experimentally, for example, with scanning electron tunneling microscopy, or with an optical Raman spectrum (since the hole localizes at a specific stacking location which might have its phonon signature).

#### ASSOCIATED CONTENT

## S Supporting Information

Moiré patterns with different relative angle  $\theta$  between the two atomic layers, the VBM distribution of a Moiré pattern with  $\theta$  =  $2^{\circ}$ , estimated errors induced by interpolation scheme, and the band structures and band gaps of the small systems obtained from both VASP and PEtot calculations. This material is available free of charge via the Internet at http://pubs.acs.org.

## AUTHOR INFORMATION

## **Corresponding Author**

\*E-mail: lwwang@lbl.gov.

#### Notes

The authors declare no competing financial interest.

## ACKNOWLEDGMENTS

This work was supported by the Theory of Materials program, funded by the Director, Office of Science (SC), Basic Energy Science (BES)/Material Science and Engineering Division (MSED) of the U.S. Department of Energy (DOE) under the contract no. DE-AC02-05CH11231. It used resources of the National Energy Research Scientific Computing Center (NERSC) and Oak Ridge Leadership Computing Facility (ORLCF) that are supported by the Office of Science of the U.S. Department of Energy, with the computational time allocated by the Innovative and Novel Computational Impact on Theory and Experiment (INCITE) project.

#### REFERENCES

(1) Radisavljevic, B.; Radenovic, A.; Brivio, J.; Giacometti, V.; Kis, A. *Nat. Nanotechnol.* **2011**, *6*, 147.

- (2) Mak, K. F.; Lee, C.; Hone, J.; Shan, J.; Heinz, T. F. Phys. Rev. Lett. **2010**, 105, 136805.
- (3) Splendiani, A.; Sun, L.; Zhang, Y.; Li, T.; Kim, J.; Chim, C.-Y.; Galli, G.; Wang, F. *Nano Lett.* **2010**, *10*, 1271–1275.
- (4) Tongay, S.; Zhou, J.; Ataca, C.; Lo, K.; Matthews, T. S.; Li, J.; Grossman, J. C.; Wu, J. Nano Lett. 2012, 12, 5576-5580.
- (5) Zeng, H.; Dai, J.; Yao, W.; Xiao, D.; Cui, X. Nat. Nanotechnol 2012, 7, 490.
- (6) Wang, Q. H.; Kalantar-Zadeh, K.; Kis, A.; Coleman, J. N.; Strano, M. S. Nat. Nanotechnol. **2012**, 7, 699–712.
- (7) Coleman, J. N.; et al. Science 2011, 331, 568-571.
- (8) Zeng, Z.; Yin, Z.; Huang, X.; Li, H.; He, Q.; Lu, G.; Boey, F.; Zhang, H. Angew. Chem., Int. Ed. 2011, 50, 11093–11097.
- (9) Dean, C. R.; Young, A. F.; Meric, I.; Lee, C.; Wang, L.; Sorgenfrei, S.; Watanabe, K.; Taniguchi, T.; Kim, P.; Shepard, K. L.; Hone, J. Nat. Nanotechnol. 2010, 5, 722.
- (10) Xue, J.; Sanchez-Yamagishi, J.; Bulmash, D.; Jacquod, P.; Deshpande, A.; Watanabe, K.; Taniguchi, T.; Jarillo-Herrero, P.; Leroy, B. J. *Nat. Mater.* **2011**, *10*, 282–285.
- (11) Yang, W.; Chen, G.; Shi, Z.; Liu, C.-C.; Zhang, L.; Xie, G.; Cheng, M.; Wang, D.; Yang, R.; Shi, D.; Watanabe, K.; Taniguchi, T.; Yao, Y.; Zhang, Y.; Zhang, G. *Nat. Mater.* **2013**, *12*, 792–797.
- (12) Lin, Q.; Smeller, M.; Heideman, C. L.; Zschack, P.; Koyano, M.; Anderson, M. D.; Kykyneshi, R.; Keszler, D. A.; Anderson, I. M.; Johnson, D. C. Chem. Mater. 2010, 22, 1002–1009.
- (13) Geim, A. K.; Grigorieva, I. V. Nature 2013, 499, 419-425.
- (14) Trambly de Laissardiere, G.; Mayou, D.; Magaud, L. *Nano Lett.* **2010**, *10*, 804–808.
- (15) Li, X. D.; Yu, S.; Wu, S. Q.; Wen, Y. H.; Zhou, S.; Zhu, Z. Z. J. Phys. Chem. C 2013, 117, 15347–15353.
- (16) Kośmider, K.; Fernández-Rossier, J. Phys. Rev. B 2013, 87, 075451.
- (17) Bernardi, M.; Palummo, M.; Grossman, J. C. Nano Lett. 2013, 13, 3664-3670.
- (18) Bertolazzi, S.; Krasnozhon, D.; Kis, A. ACS Nano 2013, 7, 3246-3252.
- (19) Terrones, H.; Lopez-Urias, F.; Terrones, M. Sci. Rep. 2013, 3, 1549.
- (20) Kou, L.; Frauenheim, T.; Chen, C. J. Phys. Chem. Lett. 2013, 4, 1730–1736.
- (21) Kresse, G.; Hafner, J. Phys. Rev. B 1993, 47, 558-561.
- (22) Kresse, G.; Furthmüller, J. Phys. Rev. B 1996, 54, 11169-11186.
- (23) Perdew, J. P.; Burke, K.; Ernzerhof, M. Phys. Rev. Lett. 1996, 77, 3865–3868.
- (24) Monkhorst, H. J.; Pack, J. D. Phys. Rev. B 1976, 13, 5188-5192.
- (25) Grimme, S. J. Comput. Chem. 2006, 27, 1787-1799.
- (26) Bučko, T.; Hafner, J.; Lebègue, S.; Ángyań, J. G. J. Phys. Chem. A 2010, 114, 11814–11824.
- (27) Sachs, B.; Wehling, T. O.; Katsnelson, M. I.; Lichtenstein, A. I. *Phys. Rev. B* **2011**, *84*, 195414.
- (28) Ramasubramaniam, A.; Naveh, D.; Towe, E. *Phys. Rev. B* **2011**, 84, 205325.
- (29) Kang, J.; Tongay, S.; Zhou, J.; Li, J.; Wu, J. Appl. Phys. Lett. 2013, 102, 012111.
- (30) Wang, L.-W.; Zhao, Z.; Meza, J. Phys. Rev. B 2008, 77, 165113.
- (31) http://cmsn.lbl.gov/html/PEtot/PEtot.html (2010).
- (32) Wang, L.-W.; Zunger, A. J. Chem. Phys. 1994, 100, 2394-2397.
- (33) MacDonald, A. H.; Bistritzer, R. Nature 2011, 474, 453-454.
- (34) Luican, A.; Li, G.; Reina, A.; Kong, J.; Nair, R. R.; Novoselov, K.
- S.; Geim, A. K.; Andrei, E. Y. Phys. Rev. Lett. 2011, 106, 126802.